ISSN 1054-660X, Laser Physics, 2008, Vol. 18, No. 3, pp. 253–262.

Conical-Wave Nonlinear Optics: From Raman Conversion to Extreme UV Generation

D. Faccio[a] and P. Di Trapani[a, b]

[a] *CNISM and Department of Physics and Mathematics, University of Insubria, Via Valleggio 11, Como, IT-22100 Italy*
[b] *Department of Quantum Electronics, Vilnius University, Sauletekio Ave. 9, bldg.3, Vilnius, LT-10222 Lithuania*
e-mail: daniele.faccio@uninsubria.it

Received September 12, 2007

Abstract—Conical waves (CW) are a particular class of wavepackets that exhibit the notable feature of being stationary solutions for both linear and nonlinear propagation equations. The possibility of independently tuning the phase and group velocities of a CW is a unique feature that opens the possibility of a number of applications, in particular, we shall consider frequency conversion processes and divide the discussion into two parts: group velocity (GV)-matched and phase-matched nonlinear processes. As a GV-matched process, we consider stimulated raman scattering within optical filaments and we highlight the role of cross-phase modulation in the formation of GV-matched X-wave pulses, leading to high Raman conversion efficiencies and the formation of 15-fs compressed pulses. Conical waves, in particular, pulsed-Bessel beams, are then considered for phase-matching higher-order harmonic generation in the extreme UV region.

PACS numbers: 43.65.-k, 42.65.Ky

DOI: 10.1134/S1054660X08030110

1. INTRODUCTION

Conical waves (CW) are a particular class of wavepackets that exhibit the notable feature of being stationary solutions for both the linear and nonlinear propagation equations. The simplest example of a CW is the monochromatic Bessel, or Durnin, beam that may be understood as the superposition of an infinite number of plane waves each with the wavevector aligned along a conical surface (hence, the origin of the name "conical waves"). The interference of these plane waves leads to the characteristic Bessel profile with a central peak that does not suffer diffraction during propagation. In the polychromatic case, the cone angle of each wavelength may be chosen so as to also cancel out the pulse dispersion, hence the property of stationarity. In the normal group-velocity dispersion regime, these stationary pulses are referred to as X waves due to their characteristic hyperbolic or X-shaped profile. A particularly convenient representation of conical waves is given in the Fourier ($k_\perp$, ω) space

$$k_\perp = \sqrt{k^2 - k_z^2}$$
$$\text{with} \quad k_z = (k_0 - \beta) + (k_0' - \alpha)\Omega, \tag{1}$$

where $k = \omega n(\omega)/c$, $k_0 = k(\omega_0)$, k_0' is the first derivative of $k(\omega)$ evaluated at ω_0, $\Omega = \omega - \omega_0$, and the two free parameters β and α are corrections to the phase and group velocity, respectively. The possibility of independently tuning the phase and group velocities of a CW through the parameters β and α is a unique feature that opens the possibility of a number of applications. In particular, we shall consider frequency conversion processes and divide the discussion into two parts:

(a) Group velocity-matched nonlinear processes:

Stimulated Raman scattering (SRS) is a nonlinear process mediated by molecular vibrations through which an intense pump wave is frequency downshifted. Phase-matching does not play a role since momentum conservation is automatically conserved in this process, while a strong limitation to the conversion efficiency may arise due to the group-velocity mismatch (GVM) between the pump and Stokes pulses. We study the problem of SRS conversion in a particular case, namely, that of ultrashort laser-pulse filamentation. Indeed, filamentation is, in principle, a particularly favorable regime in which to perform nonlinear frequency conversion due to the extremely high conversion peak intensities reached within the filament (~TW/cm^2 in condensed media) and also due to the long diffraction-free propagation of the intense central spike characteristic of all filaments. We show that a second weak-seed pulse in the presence of the intense filament suffers a strong spatiotemporal reshaping due to the effect of cross-phase modulation (XPM). The input Gaussian seed pulse is reshaped into a stationary X wave that has the same group velocity of the intense pump pulse. This remarkable discovery naturally leads to the result of an extremely efficient SRS amplification of the seed when this is tuned to the Stokes wavelength. For example, due to the reshaping of a 500-fs input seed into an X wave with the same group velocity of the pump, SRS amplification occurs over many (>5) walkoff lengths and we consequently observe strong pump depletion (>50% conversion efficiency) with the

final formation of ~50-fs intense (equal to the pump) Raman X waves.

(b) Phase-matched nonlinear processes:

In general, all nonlinear frequency conversion processes such as second- or third-harmonic generation, greatly benefit from phase matching. In the presence of a phase mismatch Δk, the power in the harmonic will oscillate along the propagation between zero and some maximum (but typically small) value with a periodicity determined by the coherence length $l_c = \pi/|\Delta k|$. Recent developments in the regime of higher-order harmonic generation that extend the laser wavelength into the extreme UV (EUV) 1–50-nm regime have attracted much interest due to possible applications such as attosecond spectroscopy and high-resolution microscopy. One of the major issues limiting the conversion efficiency into the EUV range is the presence of a phase mismatch. Various techniques have been proposed to improve the performance of a Gaussian pump pulse by modification of the effective wavevector such as the use of hollow waveguides or periodically modulated waveguides. These, however, may be used only in certain regimes due to the relatively small correction to the pump wavevector. We propose a new approach based on CWs: the β parameter that corrects the pump wavevector may, in principle, have any desired sign or magnitude and, thus, correct arbitrarily large Δk. We show results for the specific case of a pump pulse with an intensity below the so-called critical ionization threshold, so that $\Delta k > 0$. In this case, Bessel pulses are perfectly suited for the purpose. Numerical simulations and the investigation of the resulting coherence length distribution (across the pulse transverse dimension) show that the use of correctly tuned Bessel pulses leads to EUV conversion efficiencies ≥2 orders of magnitude larger than that obtainable with an equivalent (same energy and intensity) Gaussian pulse.

2. GROUP VELOCITY-MATCHED NONLINEAR INTERACTIONS WITHIN ULTRASHORT LASER-PULSE FILAMENTS

Ultrashort laser-pulse filamentation is an extremely rich branch of nonlinear optics that has been attracting interest for many years now [1] due to both the fundamental physical implications and the potential applications ranging from spectral superbroadening [2] and remote sensing [3], lightning protection [4] and, more recently, frequency conversion [5–7]. It has also been shown that the filament dynamics in condensed media with normal group-velocity dispersion (GVD) may be understood in terms of the spontaneous formation and successive interaction of nonlinear X waves [8, 9].

Optical filaments also exhibit certain features that render them very attractive for efficient frequency conversion, opening the possibility for what may be called "nonlinear filamentation optics" [6]. The main features motivating this interest may be listed as follows:

(i) high intensities over very large propagation distances. Contrary to the behavior of Gaussian pulses, the high (~TW/cm^2 in condensed media) intensity peaks that form within a filament propagate without diffraction over many Rayleigh lengths. This drastically increases the efficiency of many nonlinear processes in a way very similar to that observed in optical fibers [10].

(ii) the drastic improvement in beam quality and energy stability of newly generated frequencies [6, 11, 12] promising an increase in the pulse quality in contrast to the reduction of the pulse quality usually encountered, for example, in standard (i.e., based on Gaussian beams) parametric generators.

Clearly, a detailed understanding of the dynamics that controls the ultrashort pulse interactions with media is necessary to take advantage of these properties in practical applications. We study femtosecond filamentation in condensed media (water, ethanol) in situations where a high-power pulse (pump) interacts with a relatively weak "seed" pulse.

First, we briefly recall the nonlinear X-wave formation, and the role self- and cross-phase modulations play in it. Together with four-wave mixing processes, these are the building blocks to understanding the complete picture of the two-pulse filamentation. The notion of group velocity matching plays the central role in the X-wave formation described below. This is a general property of conical waves that makes it possible to construct localized wavepackets centered at different frequencies that nevertheless propagate with the same group velocity. This, in turn, leads to long effective interaction distances between different-color pulses and, consequently, to a high efficiency of nonlinear processes.

The specific shape and details of the conical wave as expressed in Eq. (1) depend on the refractive index dispersion relation $n = n(\omega)$ and on the values of β and α. Typically, in optical filaments in the normal GVD regime, we will observe X waves that have one of the hyperbolic tails that pass through the input pump carrier frequency at $k_\perp = 0$, so that $\beta \sim 0$ [9, 13], while the value of α, i.e., of the axial component of the group velocity $v_g = 1/(k_0' - \alpha)$, depends on the specific input conditions. We note that, if we take $\beta = 0$, the second relation in Eq. (1) may be rewritten as $k_z = k_0 + \Omega/v_g$ and is formally identical to the phase matching relation of the "effective three-wave mixing" (ETWM) model introduced by Kolesik et al. [25] and used to explain optical filamentation as a dynamical interaction between spontaneously formed X waves [8, 15].

An intense laser pulse propagating in a Kerr medium will undergo a spectral broadening due to the intensity dependence of the refractive index. In general, the nonlinear material polarization may be written as $P_{NL} \propto \chi^{(3)}EEE$, where the tensor $\chi^{(3)}$ describes the Kerr nonlinearity and E is the electric field. In the presence

of an intense pump field E_P and a weaker seed field E_S oscillating at frequencies ω_P and ω_S, respectively, the total field becomes $E = 1/2\{|E_P|\exp[i(k_P z - \omega_P t)] + |E_S|\exp[i(k_S z - \omega_S t)]\} + \text{c.c.}$ Substituting the entire field into the relation for the nonlinear polarization and retaining only the terms that oscillate with frequency ω_S, we obtain $P_{NL} \propto \chi^{(3)}(|E_S|^2 + 2|E_P|^2)E_S$. The first term describes the self-phase modulation of the seed and may be neglected if the seed field is indeed weak. On the other hand, the second term describes the cross-phase modulation, i.e., the phase modulation induced upon the weak-seed wave by the intense pump wave. The material polarization wave will, therefore, emit an electric field that oscillates with frequency ω_S: this process may thus be viewed as a three-wave scattering process in which the weak input seed field is scattered by the material polarization wave. In order to evaluate how the seed is modified, we consider the energy and momentum conservation. We note that the pump field, and, thus, the material polarization wave, may be tightly localized both in space and time as is the case, for example, within an ultrashort laser-pulse filament. A transverse spatial dimension d implies a transverse momentum spread on the order of $\Delta k_\perp \sim \pi/d$, which, in turn, implies that, for a tightly localized pump pulse, transverse momentum conservation can always be satisfied [16, 17]. A similar reasoning may also be applied to the energy conservation constraint. In other words, the tightly localized polarization wave may scatter a weak input seed pulse, approximated by a plane monochromatic wave with a transverse wavevector and frequency $(0, \omega_S)$, into an output wave with $(k_\perp, \omega)$ as long as $\omega - \omega_S$ is smaller than the inverse of the subpulse duration. Therefore, only the longitudinal k_z momentum conservation needs to be imposed explicitly and leads to

$$K_z(\omega, k_\perp) = K_z(\omega_S, 0) - \frac{\omega_S - \omega}{v_{pol}}, \qquad (2)$$

where the polarization perturbation velocity is given by the pump group velocity $v_{pol} = v_{g,p}$, and $K_z(x, y) \equiv \sqrt{(xn(x)/c)^2 - y^2}$ is a function giving the z component of the wavevector for a given frequency and transverse wavenumber. The important point here is that Eq. (2) is identical to the relation in Eq. (1) (with $\beta = 0$) and we may, therefore, conclude that XPM tends to reshape the input Gaussian spectrum into that of a stationary conical wave. In other words, in the normal GVD regime, the input Gaussian seed is expected to develop a marked conical emission (CE) pattern, induced by XPM and with an angular dispersion that will support nondispersive propagation. Furthermore, comparing Eq. (2) with Eq. (1), we observe that the XPM-induced conical emission will travel at the group velocity $v_{g,p}$ of the source *pump* pulse.

We have verified the scenario sketched in this section both numerically and experimentally. Numerical simulations were carried out using two independent codes, hereafter described as the KO code and the CO code. The KO code was written by Kolesik and is based on an unidirectional pulse-propagation equation, the derivation of which is presented in [22, 23]. The CO code was written by Couairon and solves the nonlinear equation for the envelope $\mathcal{E}_{\omega,r,z} = \mathcal{F}(\mathcal{E}_{t,r,z})$, where $\mathcal{F}$ denotes the Fourier transform and the laser field with central frequency ω_0 reads as $E_{t,r,z} = \mathcal{E}_{t,r,z}\exp(-i\omega_0 t + ik_0 z)$. The derivation of the envelope equation used in the CO code from the wave equation in nonlinear media is recalled in [1, 24]. We refer the reader for more details regarding these codes, to the parameters used in this work, and in the comparison between the results obtained with the two codes to [19]. Overall, the agreement between theory and experiment is extremely good and we can, thus, propose a coherent, self-consistent experimental–theoretical picture for the two-pulse filamentation in the presence of resonant energy exchange. The experiments were carried out using a frequency-doubled Nd:glass amplified laser (Twinkle, Light Conversion Ltd., Vilnius, Lithuania) that delivers up to 4-mJ, 1-ps, 527-nm pulses with a 10-Hz repetition rate. The laser pulses were loosely focused by a 50-cm lens, down to a 90-μm FWHM diameter onto the input facet of a 4-cm-long fused silica cuvette containing pure water. Part of the energy of the pump pulse is split before focusing and used to pump a parametric amplifier (TOPAS, Light Conversion Ltd., Vilnius, Lithuania). The output of the amplifier after further frequency doubling is a 490-fs pulse, tunable in the 400–700 nm wavelength range. This pulse is used as the seed in our experiments: its energy is limited to 250 nJ and is focused onto the water cuvette with a larger 200-μm FWHM diameter. The temporal overlap between the pump and seed pulses is controlled by a variable delay line. The output from the water cuvette was collected with $f = 5$ cm achromat lens. At a distance f after the lens, we placed an imaging spectrometer so that, at the output, we recover the full (θ, λ) spectrum [7, 14]. The spectrum is then recorded by using a CCD, either a 16-bit Andor iDus or a color Nikon D70 camera that has been modified so as to extend the visibility range from 350 to 1100 nm [18]. It has been shown that the (θ, λ) spectrum may be used to determine the group velocity of a generic pulse [7, 9, 15] and the detailed recipe used in this work is given in [19, 20].

Figure 1 shows the spectrum measured with a 2-μJ pump pulse and a weak 250-nJ seed pulse centered at 490 nm. The pump pulse has formed a filament within the water sample, thus generating the clear blue and red-shifted CE tails that are visible around the central pump wavelength. The seed pulse also shows a clear blue-shifted CE tail. For comparison, the inset shows the same spectrum, but with a lower 1-μJ pump pulse energy. The pulse has not formed a filament, so that the

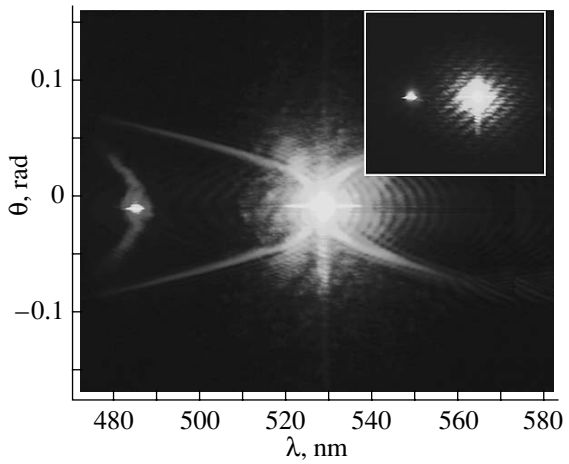

Fig. 1. Spatiotemporal modification of a weak 250-nJ 490-nm seed pulse in the presence of an intense 2-μJ 527-nm pump pulse. The inset shows the experimental spectrum taken at a lower 1-μJ input pump energy, i.e., in the absence of nonlinear interactions.

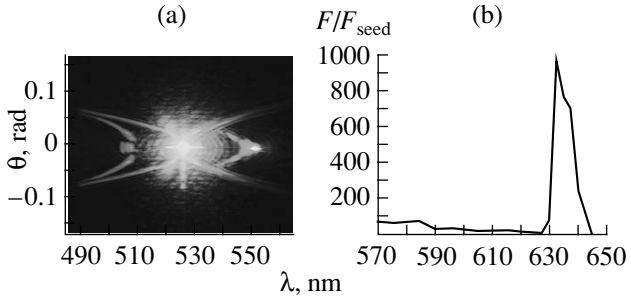

Fig. 2. (a) Experimentally measured spectrum with a 550-nm seed pulse that is reshaped into an X wave through XPM and amplified and converted to ~505 nm through FWM. (b) Measured peak fluence amplification of the seed pulse as the wavelength is tuned from 570 to 650 nm.

pump peak intensity is much lower, and no nonlinear effects are taking place. Using the Sellmeier relation for water taken from [21, Eq. (12)], we evaluate the group velocities related to the blue-shifted CE tails originating from the pump as $v_{g,p1} = 2.240 \pm 0.005 \times 10^8$ m/s, while the red-shifted CE tails give $v_{g,p2} = 2.180 \pm 0.006 \times 10^8$ m/s. The small deviation around the mean value indicates that the group velocity has no wavelength dependence, i.e., the pulse is nondispersive as expected for a stationary X wave. As for the seed pulse CE, this has a group velocity $v_{g,s} = 2.26 \pm 0.06 \times 10^8$ m/s that is equal, within the experimental error, to $v_{g,p1}$, which may be interpreted as being due to the formation of a stationary X pulse at the seed wavelength induced by XPM. We underline that this process does not necessarily require an X pulse or a filament at the pump wavelength, but only a very intense and tightly focused peak (although it is clear that the filament is a very practical way to achieve such conditions).

We now study the effect of tuning the seed pulse wavelength either close to the pump wavelength so as to enhance additional FWM effects through a reduction of the phase mismatch, or to the Stokes wavelength so as to enable SRS amplification. Figure 2a shows an example of a spectrum measured by tuning the seed wavelength to 550 nm, while the input conditions for the pump are maintained as in Fig. 1. The conical emission is clearly visible originating from the seed signal and this is accompanied by the generation of a signal around 505 nm, which also exhibits a marked CE. The experimentally measured pump (λ_p), seed (λ_s) and blue-shifted signal (λ_b) on-axis wavelengths are linked by the relation $1/\lambda_b = 2/\lambda_p - 1/\lambda_s$, so that we ascribe this process to FWM. Similar spectra were registered when tuning the seed wavelength up to 570 nm. Figure 2b shows the gain at the seed wavelength measured as the ratio of the seed-peak fluence values before and after the water cell: A gain of a factor 80 is observed over a 55-nm bandwidth. Tuning the seed further away from the pump wavelength leads to a strong reduction of the gain due to phase mismatch. However, very strong 1000× amplification is registered around 635 nm, which corresponds very closely to the expected Stokes wavelength in water for a pump wavelength of 527 nm [16]. Furthermore, the gain curve around 635 nm is bell-shaped with a FWHM of ~200 cm^{-1}, which is also in close agreement with the SRS gain bandwidth measured by other means [16]. In [7], it was shown that this amplification process is associated with the formation of so-called Raman X waves, i.e., X waves centered at the Stokes wavelength and amplified SRS.

Furthermore, it was highlighted how the Raman and pump X waves had the same group velocity, thus explaining the large SRS gain notwithstanding the short ($\tau \sim 50$ fs) pulse durations that would otherwise be expected to give rise to very short GVM walkoff lengths, $L_{GVM} = \tau(1/v_{g1} - 1/v_{g2})^{-1} \sim 1.8$ mm (where $v_{g1,2} = dk/d\omega|_{\omega_{1,2}}$ are the group velocities of the two pulses). It is now clear that the group-velocity matching, necessary for efficient SRS amplification, is guaranteed through a XPM-induced reshaping of the seed pulse into an X wave. Figure 3a shows the measured full spectrum (from the near-UV to the near-IR region) obtained with a 2.4-μJ input pump power and a 250-nJ seed pulse tuned to 637 nm. The delay between the pump and seed pulse was optimized so as to maximize the intensity distribution in the CE tails around the Stokes wavelength. We note that, by changing the delay within a ~1000-fs range, it was possible to excite just the blue-shifted, red-shifted, or both CE tails in the same manner as reported in [7]. Figure 3b shows the numerically calculated spectrum with the same input conditions used in the experiment and simulation parameters optimized to reproduce our experimental results as described in detail in [19, 20].

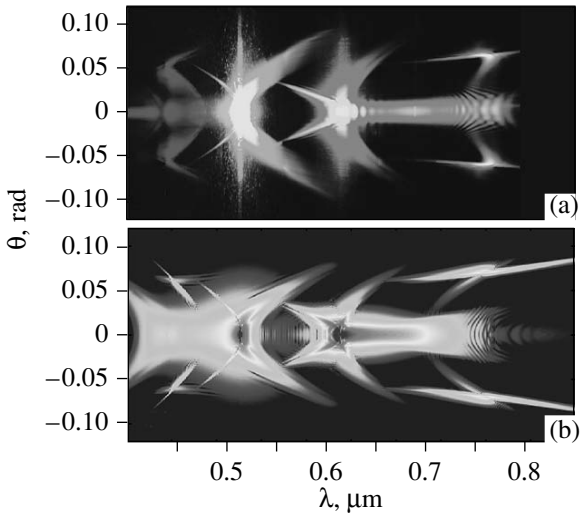

Fig. 3. (a) Measured (θ, λ) spectrum of a 2.4-μJ filament in 4 cm of water with a weak 250-nJ 637-nm seed pulse. (b) Numerical simulation (in logarithmic scale, six decades are shown) with the experimental input parameters in (a) and a 600-fs relative delay between seed and pump pulses (measured at the water-cell input facet).

The effect of the group-velocity matching may be also appreciated in the near-field axial intensity profiles shown in Fig. 4 (for the same conditions as in Fig. 3). The profiles are shown for different propagation distances z as indicated in the graphs: the blue line indicates the full intensity profile and the red line shows the intensity profile of just the Stokes pulse. The input pulse splits at $z \sim 2.5$ cm into two daughter pulses that move further apart during propagation. The underlying seed pulse splits in exactly the same fashion with each seed daughter pulse remaining "locked" to the relative pump pulse. The effect of this can be clearly seen by noting that the Stokes wavelength continues to increase in energy in a steady, uniform fashion over more than five walk-off lengths (last graph in Fig. 4).

We now focus our attention on the off-axis features present in all our spectra around the 450- and 800-nm wavelengths (e.g., Fig. 3). If we take, for example, Fig. 3a, we note relatively intense "whiskers" of light in the red-shifted 740–820-nm region and at ~±0.05 rad angles. Similar "whiskers" are also visible in the blue-shifted 400–500-nm region. These features appear only in the presence of the amplified seed pulse and are, thus, linked to the Raman X-wave formation process. These "whiskers" have been shown to be created through a phase-matched FWM process in which the interacting photons belong to the pump and Raman X waves [19, 20].

In Figs. 5a–5c, we show the on-axis intensity (NF) profiles obtained from the spectrum in Fig. 3b. In particular, we numerically performed the Fourier transform of only selected portions of the spectrum corresponding to the whiskers, so as to obtain its near-field distribution. To this end, we numerically put to zero the spectrum intensity outside the region |0.6 – 1.1| rad,

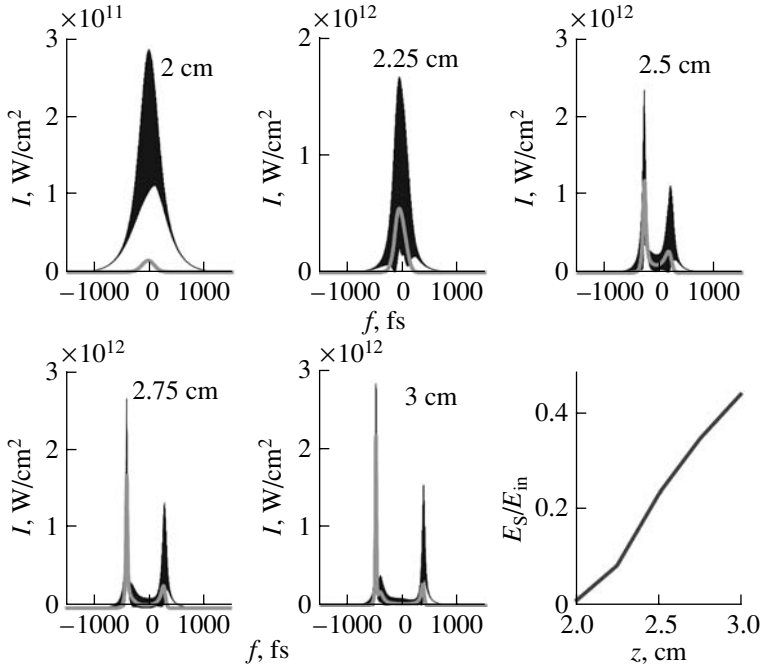

Fig. 4. Numerically simulated (CO code) on-axis temporal intensity profiles for the pump pulse (black lines) and the seed pulse (gray lines). The propagation distance z is indicated in each graph. The last graph shows the Raman gain (energy at Stokes wavelength normalized to pump energy) versus z.

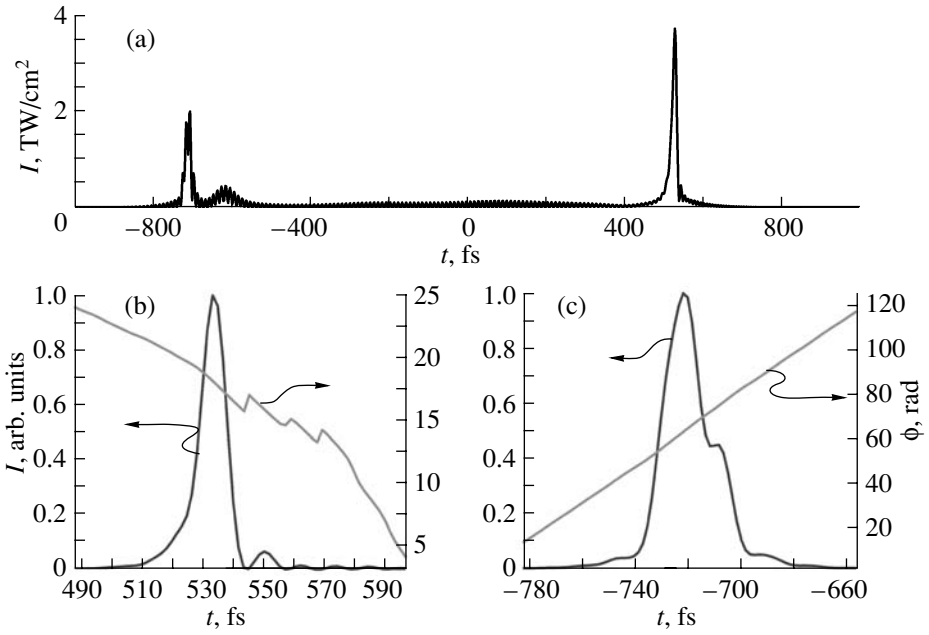

Fig. 5. Numerically simulated on-axis temporal intensity profiles of the "whisker" spectral features, (a) the unfiltered profile, (b) the red-shifted "whisker" temporal profile showing a single isolated peak with a ~15-fs duration and (c) the blue-shifted "whisker" temporal profile showing a single isolated peak with a ~8-fs duration.

700–900 nm for the red-shifted whiskers and |0.2 – 0.8| rad, 400–500 nm for the blue-shifted whiskers. Figure 5a shows the unfiltered on-axis intensity (from Fig. 5a), while Figs. 5b and 5c show the on-axis intensity profiles of the blue-shifted and red-shifted "whiskers," respectively. As can be seen, these form isolated intensity peaks with ~15- and ~8-fs FWHM durations with very limited pre- or post-pulse oscillations and ~40- and ~200-GW/cm^2 peak intensities (corresponding to energies of 2 and 20 nJ, respectively). Such pulses could be experimentally isolated by placing an annular-shaped aperture in the spatial far-field of the wavepacket. Furthermore, the same graphs show the phase profile for these profiles indicating the presence of a linear chirp. The time-bandwidth product for the blue and red-shifted "whiskers" is ~1.2 and ~1.6, respectively, indicating that a correction of the linear chirp would result in ~5-fs duration pulses.

The present results, therefore, allow us to propose a self-compression scheme leading to few-cycle pulses with unprecedented compression ratios and an excellent temporal contrast. This concludes the section regarding group velocity-matched nonlinear interactions mediated by conical waves.

3. PHASE-MATCHED HIGHER-ORDER HARMONIC GENERATION

In this section, we move on to examine the possibility of using conical waves, in particular pulsed-Bessel beams, to obtain phase-matched and, therefore, efficient frequency conversion from the laser pump pulse to higher-order harmonics extending into the extreme UV (EUV) region.

Since the beginning of the 1990s, it has been known that a crucial requirement for efficient high harmonic generation (HHG) is that of a phase-matched interaction between the pump and the harmonic field [28, 29]. Many efforts have been made in recent years to overcome the mismatch factors which still severely limit the harmonic field brightness and its use for many interesting applications. The phase mismatch Δk on axis can be expressed as [30, 31]

$$\Delta k = qk_{\text{laser}} - k_q = \frac{q2\pi(1-\eta)}{\lambda}\Delta n + P\eta N_{\text{atm}} r_e\left(\frac{\lambda}{q} - q\lambda\right) + \text{geometric term} + \text{atomic phase}, \quad (3)$$

where q is the harmonic order, λ is the laser wavelength, P, η, N_{atm}, and r_e are the gas pressure in atmospheres, the ionization fraction, the gas number density at 1 atm, and the classical electron radius, respectively, and $\Delta n = n_{\text{laser}} - n_q$. The first (positive) and second (negative) term refer to material dispersion and plasma dispersion, respectively; the geometric term has a positive sign for the focused-Gaussian geometry and is negative in a wave-guided [32] or self-guided [33] geometry, while the sign of the atomic dipole-phase term (related to the quantum paths of the electrons involved in the HHG process) is, in general, not fixed during propagation since it is proportional to dI/dz [34].

We consider the specific regime in which the material dispersion term is greater than the plasma dispersion term, i.e., below the so-called "critical ionization" limit. Hollow waveguides have been shown to give rise to phase matching in this regime; however, their application is limited to low gas pressures and they can compensate only a relatively small phase mismatch. On the contrary, we show how the appropriate choice of an apodized pulsed-Bessel beam (PBB) as a pump pulse leads to efficient phase-matching even in extreme conditions (e.g., very high gas pressures). Two properties of PBBs make them promising for HHG: first, compared to the Rayleigh range of a Gaussian pulse having the same width, the PBB is nondiffractive over a much longer distance. This, in turn, implies a propagation with a smoother intensity and phase evolution (the latter was studied in [35] in the case of severely truncated PBBs) and a less relevant role of the atomic phase and geometrical terms in Eq. (3). The second crucial property of PBB is the possibility of controlling the phase velocity by simply changing the angle of the Bessel cone. In particular, the axial wavevector k_z will always be *shortened* with respect to the plane wave k_0 by an amount β given by $\beta = k_0(1 - \cos\gamma)$, where γ is the angle of the Bessel cone. Substituting $k_z = k_0 - \beta$ into Eq. (3), we obtain for the PBB

$$\begin{aligned}\Delta k &= qk_{\text{laser}} - k_q = q(k_0 - \beta) - k_q \\ &= \frac{q2\pi(1-\eta)}{\lambda}\Delta n + P\eta N_{\text{atm}} r_e\left(\frac{\lambda}{q} - q\lambda\right) \\ &\quad + \text{atomic phase} - q\beta.\end{aligned} \tag{4}$$

The peculiar contribution given by $-q\beta$ has the same sign as the plasma dispersion term. Therefore, for pump intensities *below* the critical ionization threshold, one can think to choose a suitable β (i.e., a suitable axicon or a hologram pattern) to compensate the phase mismatch between the pump and signal. We note that the contribution to phase matching given by $-q\beta$ plays the same role as the waveguide geometric term, but in a much wider range: in waveguides, the contribution Δk scales as $1/a^2$, and with a diameter $a = 100$ μm $\Delta k \approx 36$ m^{-1}. In contrast, with a simple axicon having, for example, $\beta = 2.8°$, one obtains $\Delta k \approx 2337$ m^{-1}. A similar Δk in the hollow waveguide configuration would require use of a very narrow waveguide with $a = 12$ μm with extremely difficult alignment and energy coupling.

To numerically investigate phase matching with PBB, we adopted the well-established technique of the "coherence map," introducted by Balcou et al. [34]. Following the same approach as Tosa et al. [33], we applied this technique to the calculated solution of the pump propagation equation, which was obtained with a numerical code based on the solution of the nonlinear Schrödinger equation that properly accounts for the tunneling ionization rates and is described in detail elsewhere [1, 24] (this is the CO code referred to in the previous section). As Tosa et al. pointed out, with this procedure, all nongeometrical effects (such as plasma and material dispersion) that have a role in the phase matching are already included in the calculation and there is no need to consider them separately.

We recall very briefly to the reader that the coherence map gives the coherence length L_{coh} for the generation process of a given harmonic order q along the radial profile of the pump pulse at its intensity peak. The coherence length describes the propagation length over which the signal adds up constructively and is defined as $L_{\text{coh}} = |2\pi/\mathbf{dk}|$, where $\mathbf{dk} = 2\pi q n_q/\lambda - \mathbf{k}_{\text{pol}}$; n_q is the refractive index for the harmonic signal (taken from [36]), and $\mathbf{k}_{\text{pol}}$ is the polarization wavevector given by $\mathbf{k}_{\text{pol}} = q\nabla[\phi(r, z)] + \nabla[\alpha I(r, z)]$. Here, $\phi(r, z)$ and $I(r, z)$ are the fundamental field phase and intensity profile retrieved by the simulation, and α is the phase coefficient for the harmonic field [37]. Using this procedure, every mismatch factor in Eq. (4) is accounted for.

In order to illustrate the impact of the phase-matching capability of PBBs, we chose to study rather extreme conditions, e.g., the generation of the 61st harmonic in helium at a pressure of 1 atm. The input pump pulse parameters are taken as typical experimental conditions, i.e., an input duration of 35 fs FWHM and energy of 5 mJ. The input beam was taken to be a PBB with a cone angle of 2.8° ($\beta = 1907$ m^{-1}) corresponding to a distance of 31 μm between the first zeros. The PBB is radially apodized with a Gaussian function that has a FWHM radius of 250 μm, therefore, giving a peak intensity of 4×10^{14} W/cm^2.

As pointed out in [38, 39], the ultimate limit for HHG at a certain pump intensity is determined by the absorption of the harmonic signal in the gas described by the absorption length L_α. To enter the so-called absorption limited regime, where harmonic generation efficiency is maximized, one should ensure that $L_{\text{coh}} > 10L_\alpha$. The absorption length for the 61st harmonic in helium at a pressure of 1 atm is $L_\alpha \sim 0.82$ mm [36]; therefore, it is sufficient to optimize the PBB β or cone angle so as to obtain a coherence length of a few centimeters.

Figure 6 shows the calculated coherence length map for the given parameters, which is the result of an iterative optimization process: both the PBB angle and peak intensity enter into Eq. (4) and a variation in the PBB angle will, in turn, also vary the peak intensity. As may be seen, the coherence map exhibits a sharp peak only ~0.5-μm wide and distributed along the propagation direction z in which the coherence length L_{coh} is ≥3 cm. As a result of the nondiffractive nature of the PBB, this value is maintained over a large propagation distance.

The impact of this result is evident in Fig. 7, which shows the evolution of the harmonic power (intensity integrated over the effective area in which the harmonic is generated) estimated using the approach described in

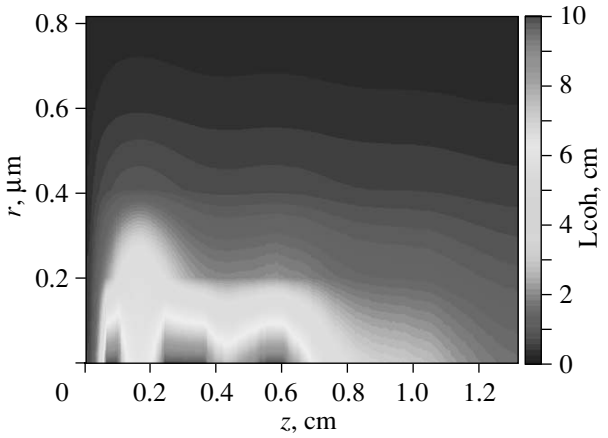

Fig. 6. Coherence length (in cm) for a Bessel pump beam in helium at a pressure of 1 atm, phase matched with the 61st harmonic over more than 1 cm of propagation.

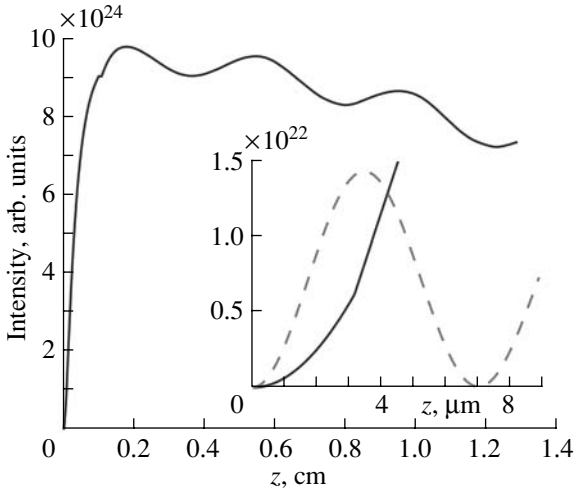

Fig. 7. Calculated power in the 61st harmonic generated in helium using a phase-matched PBB pump. The inset shows in detail the power growth in the first few microns compared to that obtained with a Gaussian pump pulse with the same input energy and peak intensity.

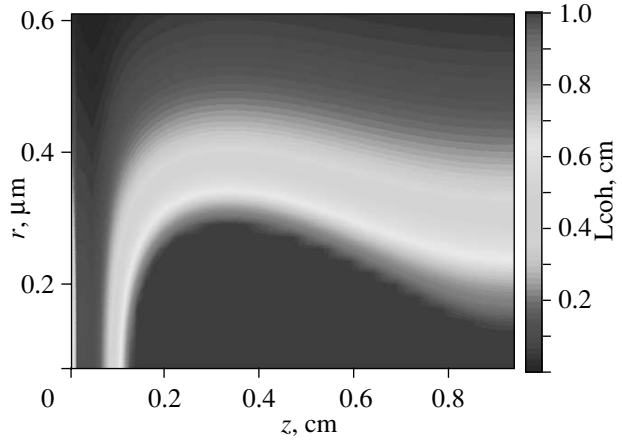

Fig. 8. Calculated coherence length map for the generation of the 27th harmonic in argon (0.2 atm pressure).

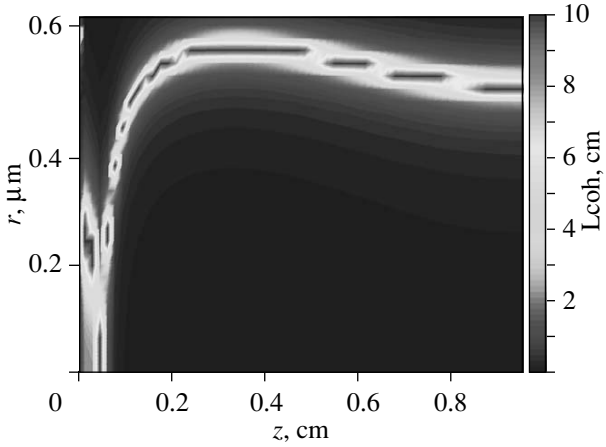

Fig. 9. Calculated coherence length map for the generation of the 29th harmonic in argon (0.2 atm pressure).

[40]. The harmonic power steadily increases until the absorption limit is reached around $z = 2$ mm. At this point, the harmonic yield saturates and attains a high value that will start to decrease (due to absorption) following the decrease of the pump pulse intensity along the propagation, which depends on the input pulse apodization width. The inset to Fig. 7 shows a detailed comparison of the harmonic power obtained by the PBB and by a Gaussian pulse with the same input duration, energy, and peak intensity of the PBB. Due to the larger width of the equivalent Gaussian pulse within which the conditions for the generation of the 61st are satisfied, the initial yield of the Gaussian pulse is higher than that of the PBB. However, the coherence length for a nonphase matched process in this regime is only ~3 μm, so that the conversion process quickly saturates and then continues to oscillate between a maximum and minimum value (generally not zero due to absorption). The overall result is, therefore, a factor of ~1000 improvement in the conversion efficiency when using the PBB with respect to the Gaussian pulse.

As a second example, we consider the generation of the 27th harmonic in argon at a pressure of 0.2 atm. In this case, the material absorption length is ~1.5 mm, which is sufficient to optimize the phase-matching length to be on the order of 1 cm. Figure 8 clearly shows that we may indeed obtain a coherence length greater than 1 cm over the whole simulated propagation length (1 cm) using a pulsed-Bessel beam with an energy of 2.6 mJ, a Gaussian apodization of 350 μm (FWHM), and a half-cone angle of 0.8°, corresponding to $\beta = 783$ m^{-1}. It is interesting to note that, for the lower

harmonics considered in this example, the coherence length has a slightly less critical dependence on the parameters, so that, with the same arrangement, we now also observe phase matching at successive higher-order harmonics. In particular, Fig. 9 shows the coherence map for the 29th harmonic. This wavelength is no longer phase matched on-axis, but rather on a ring centered on the propagation axis and well separated from the 27th harmonic. This, therefore, opens the possibility of observing multiply phase-matched harmonics within the same experiment with the possibility of spatially separating each harmonic order.

4. CONCLUSIONS

In conclusion, we have shown how, under conditions of extreme spatiotemporal focusing, a laser pulse may reach intensities high enough to induce strong XPM effects on a much weaker seed pulse. XPM will, thus, induce conical emission on the seed pulse that may be interpreted as a spontaneous transformation of the seed pulse into a stationary X wave. This finding provides an interpretation and model for those nonlinear interactions such as FWM, third-harmonic generation, or SRS that may occur within filaments in both condensed and gaseous media. In particular, we focused attention on the case of a large material gain, i.e., SRS, such that the XPM-induced seed X wave is efficiently amplified. The large conversion efficiencies may be explained as a result of the group-velocity matching between the pump and Raman X pulses. This is a unique feature of conical pulses: if the interacting pulses were Gaussian, then the group velocities would be determined by the carrier wavelengths (and material dispersion at these wavelengths) and the GVM would severely limit SRS. On the other hand, X-waves sustain a central intensity spike that may travel at any given group velocity and, thus, effectively cancel any GVM. This finding may, in principle, be extended also to gaseous media: filamentation in gases leads to the formation of 10–100 TW/cm^2 intensity peaks, so that, although the Raman gain is typically an order of magnitude smaller than in water, Raman X formation should maintain the same efficiency as that demonstrated in this work.

The (θ, λ) spectra also reveal the presence of FWM between the pump and Raman X wave conical tails that leads to the formation of spectrally extended "whisker" features. By isolating these features, it is possible to generate ultrashort clean ~8–15-fs pulses with pump pulse durations of 1 ps and possibly longer. Such pulses could be used, for example, for further amplification through chirped-pulse optical-parametric amplification ([26, 27]) and the generation of TW power pulses. The use of such seed pulses would imply the notable advantage of a single laser providing both high-quality seed and pump pulses and, thus, eliminating the requirement to synchronize different laser sources. Finally, we have shown that, by the appropriate choice of the pulsed-Bessel beam parameters, it is possible to effectively phase match higher-order harmonic generation, even in extreme conditions in which other techniques based, for example, on hollow waveguides or periodically modulated waveguides for quasi-phase matching would fail. Moreover, since the harmonic signal remains high over a reasonable distance of several millimeters once reached, the absorption limit is reached, and the experimental realization with a gas cell should be easily feasible. The technique can be applied to other operating conditions (i.e., any desired harmonic order for any particular gas) as long as the pump pulse remains below the critical ionization threshold; in particular, it may be of great interest in the spectral region below 10 nm, where, to the best of our knowledge, the absorption limit has never been reached. Over the critical ionization limit, we expect the same results to be attainable with X waves that have the advantage with respect to PBB of a tunable β that may assume either negative (as the PBB) or positive values.

ACKNOWLEDGMENTS

The authors wish to thank A. Couairon and M. Kolesik for providing their codes and help in the numerical simulations The authors also wish to acknowledge support from: the Consorzio Nazionale Interunversitario per le Scienze della Materia (CNISM)—progetto INNESCO; the Italian Ministry for Research (MIUR)—PRIN 2005; and Access to Research Infrastructures Activity in the Sixth Framework Programme of the EU (contract no. RII3-CT-2003-506350, Laserlab Europe). PDT acknowledges support from the Marie Curie Chair Project STELLA, contract no. MEXC-CT-2005-025710.

REFERENCES

1. A. Couairon and A. Mysyrowicz, Phys. Rep. **441**, 47 (2007).
2. R. R. Alfano, *The Supercontinuum Laser Source* (Springer, New York, 1989).
3. P. Rairoux, H. Schillinger, S. Niedermeier, et al., Appl. Phys. B **71**, 573 (2000).
4. M. Rodriguez, R. Sauerbrey, H. Wille, et al., Opt. Lett. **27**, 772 (2002).
5. F. Théberge, N. Aközbek, W. Liu, et al., Phys. Rev. Lett. **97**, 0239041 (2006).
6. S. L. Chin, F. Théberge, and W. Liu, Appl. Phys. B **86**, 477 (2007).
7. D. Faccio, A. Averchi, A. Dubietis, et al., Opt. Lett. **32**, 184 (2007).
8. M. Kolesik, E. M. Wright, and J. V. Moloney, Phys. Rev. Lett. **92**, 253901 (2004).
9. D. Faccio, M. A. Porras, A. Dubietis, et al., Phys. Rev. Lett. **96**, 1939011 (2006).
10. G. Agrawal, *Nonlinear Fiber Optics* (Academic, New York, 1989; Mir, Moscow, 1991).

11. B. Prade, M. Franco, A. Mysyrowicz, et al., Opt. Lett. **31**, 2601 (2007).
12. T. Pfeifer, L. Gallmann, M. J. Abel, et al., Opt. Lett. **31**, 2326 (2006).
13. C. Conti, Phys. Rev. E **70**, 0466131 (2004).
14. D. Faccio, P. Di Trapani, S. Minardi, et al., J. Opt. Soc. Am. B **22**, 862 (2005).
15. M. Kolesik, E. M. Wright, and J. V. Moloney, Opt. Express **13**, 10729 (2005).
16. M. Wittmann and A. Penzkofer, Opt. Commun. **126**, 308 (1996).
17. D. Faccio, A. Averchi, A. Couairon, et al., Phys. Rev. E **74**, 0476031 (2006).
18. Commercial CCD cameras come equipped with a limiting spectral filter in front of the CCD. This may be removed and substituted with a clear glass. For more details see http://www.lifepixel.com/IR.htm.
19. D. Faccio, A. Averchi, A. Couairon, et al., Opt. Express (in press) (2007).
20. D. Faccio, A. Couairon, P. Di Trapani, *Conical Waves, Filaments and Nonlinear Filamentation Optics* (Aracne, Rome, 2007).
21. A. G. Van Engen, S. A. Diddams, and T. S. Clement, Appl. Opt. **37**, 5679 (1998).
22. M. Kolesik, J. V. Moloney and M. Mlejnek, Phys. Rev. Lett. **89**, 2839021 (2002).
23. M. Kolesik and J. V. Moloney, Phys. Rev. E **70**, 0366041 (2004).
24. A. Couairon, E. Gaižauskas, D. Faccio, et al., Phys. Rev. E **73**, 0166081 (2006).
25. M. Kolesik, G. Katona, J. V. Moloney, and E. M. Wright, Appl. Phys. B **77**, 185 (2003).
26. A. Dubietis, R. Butkus, and A. Piskarskas, IEEE J. Sel. Top. Quantum Electron. **12**, 163 (2006).
27. N. Ishii, L. Turi, V. S. Yakovlev, et al., Opt. Lett. **30**, 567 (2005).
28. A. L'Huillier, K. J. Schafer, and K. C. Kulander, Phys. Rev. Lett. **66**, 2200 (1991).
29. P. Balcou and A. L'Huillier, "Phase-Matching Effects in Strong-Field Harmonic Generation," Phys. Rev. A **47**, 1447 (1993).
30. T. Pfeifer, C. Spileman, and G. Gerber, Rep. Prog. Phys. **69**, 443 (2006).
31. A. Paul, E. Gibson, X. Zhang, et al., IEEE J. Quantum Electron. **42**, 14 (2006).
32. C. G. Durfee, A. R. Rundquist, S. Backus, et al., Phys. Rev. Lett. **83**, 2187 (1999).
33. V. Tosa, E. Takahashi, Y. Nabekawa, and K. Midorikawa, Phys. Rev. A **67**, 063817 (2003).
34. P. Balcou, P. Salieres, A. L'Huiller, and M. Lewenstein, Phys. Rev. A **55**, 3204 (1997).
35. C. Altucci, R. Bruzzese, D. D'Antuoni, et al., J. Opt. Soc. Am. B **17**, 34 (2000).
36. www-cxro.lbl.gov.
37. M. Lewenstein, P. Saliéres, and A. L'Huillier, Phys. Rev. A **52**, 4745 (1995).
38. E. Constant, D. Garzella, P. Breger, et al., Phys. Rev. Lett. **82**, 1668 (1998).
39. M. Schnürer, Z. Cheng, M. Hentschel, et al., Phys. Rev. Lett. **83**, 722 (1999).
40. Y. Tamaki, J. Itatani, M. Obaro, and K. Midorikawa, Phys. Rev. A **62**, 063802 (2000).